17th World Conference on Earthquake Engineering, 17WCEE
Sendai, Japan - September 13th to 18th 2020

EXPERIMENTAL AND COMPUTATIONAL RESEARCH INTO THE LOWER DAMAGE STATE DS1 FOR MASONRY STRUCTURES

P.A. Korswagen[(1)], M. Longo[(2)], J.G. Rots[(3)],

[(1)] *Researcher, Section of Structural Mechanics, Delft University of Technology, Netherlands, P.A.Korswagen@tudelft.nl*
[(2)] *Researcher, Section of Structural Mechanics, Delft University of Technology, Netherlands, M.Longo@tudelft.nl*
[(3)] *Professor, Section of Structural Mechanics, Delft University of Technology, Netherlands, J.G.Rots@tudelft.nl*

Abstract

In recent years, gas extraction in the northern part of the Netherlands bas been causing low-magnitude, induced, shallow earthquakes. Besides safety and 'near collapse' limit states the lower damage state, DS1, is important. Multiple light earthquakes may produce 'light' damage in the form of cracks in masonry houses. This gives societal unrest, serviceability losses and uneasy claiming procedures of individual people against oil companies and government.

An experimental and numerical campaign is ongoing at Delft University of Technology, aiming to improve the knowledge of the underlying physics of crack initiation, propagation and snap-through in unreinforced masonry structures typical in the Netherlands. First, a damage scale and scalar damage parameter are defined herein in order to objectively quantify cracking damage as a function of the number, length, and width of cracks in masonry walls. Next, the cracking mechanisms are studied experimentally for walls and spandrels subjected to in-plane loading. High-resolution Digital Image Correlation is used to accurately detect crack formation and the evolution of the crack pattern. The experimental results will be interpreted towards drift values corresponding to various levels of the damage parameter that coincide with subdivisions of DS1.

Subsequently, orthotropic macro composite continuum models will be tuned and validated against the test results. Constitutive improvements will be made, including different unloading/reloading schemes for the mode-I tensile, mode-II Coulomb friction and compression domain respectively. With these validated models extrapolations to real building cases have been made, examples of which are included. The combination of existing damage due to e.g. differential settlement, restrained shrinkage and new damage due to seismicity will be reflected upon.

Keywords: Damage, Unreinforced masonry, Nonlinear finite element analysis, Cracking, Induced seismicity, Lab tests

1. Introduction

The extraction of natural gas in the north of the Netherlands has led to induced seismic events that are suspected to have caused damage to the buildings in the region [1]. The possibility of strong earthquakes, capable of generating severe structural damage, led in turn to an extensive study and characterisation of the (potential) events and the ultimate-limit-state resistance of the exposed structures as detailed for instance in van Elk et al. [2], who discuss the multiple steps between assessing seismicity and building fragility; Messali et al. [3], who present a multi-scale approach towards characterising the ultimate limit state of Dutch masonry structures; Esposito et al. [4], who performed quasi static pushover tests on a full scale clay masonry structure; or Graziotti et al. [5], who conducted dynamic tests of similar structures. Nonetheless, the more frequent, lighter events, occurred to date and likely to occur in the future, are most to blame for the economical losses, societal unrest, and, what can be denoted, 'light damage' to the vulnerable, unreinforced masonry structures, common in the region. The serviceability limit state of these structures requires thus further study.

The Dutch masonry structures, with slender walls, large opening, simple connections, and no seismic-design, are sufficiently unique that no comparable structures are found in other seismic countries. Moreover, the high sensitivity of the 'light damage' to the material properties, structural configuration, repeated vibrations, and existing conditions, such as prior (differential) settlement deformations, make the evaluation of the damage more complex. Furthermore, unlike near-collapse evaluations, where the characterisation of the damage can be performed using a parameter linked to structural behaviour, such as inter-storey drift, the characterisation of 'light damage' is more aesthetic and can be highly dependent on the progression of the damage due to multiple seismic events. Some studies [6, 7, 8] do observe and categorise damage, but don't consider the its propagation in quantifiable detail.

It is in this context that a study into the serviceability behaviour of Dutch masonry and the initiation and progression of 'light damage' has been conducted in the past three years at the Delft University of Technology. Herein presented is a summary of the main observations regarding light damage as obtained from this study concerning experimental tests and computational finite element models and simulations.

First, however, a few limitations must be mentioned. Foremost, a simultaneous field-case-based study into the origins of the damage [9], revealed that existing damage seemed to be limited to in-plane actions. Therefore, the investigations into light damage have focused so far only on in-plane actions and 2D effects. While out-of-plane actions are extremely relevant for assessing the ultimate-limit-state of the structures, these actions have been neglected here for the serviceability state. Secondly, some observations are yet to be compared against field measurements, and these, incorporated into models and simulations. Finally, albeit an extensive material characterisation campaign has allowed the study of relevant masonry types, the myriad of masonry configurations presents limits to these observations.

So, this paper details the three-tiered approach employed to quantify light damage in Dutch masonry structures exposed to induced earthquakes. First, experiments are used to get a glimpse into the light damage behaviour and calibrate finite element models capable of replicating masonry in terms of strength, stiffness, hysteresis and damage. Then, the models are extrapolated to simulate the impact of (repeated) seismic events and a relationship with light damage is established. Finally, this relationship is employed to compute the probability of light damage for different intensities of events. Yet, a first step is to define the nature of light damage.

2. Definition and Quantification of Light Damage

It is difficult to characterise light damage without first defining it properly, and it is almost impossible to quantify its progression without having a precise denotation for it. Qualitative descriptions of damage are too vague to be able to monitor the progression of damage unless the damage increases significantly. It is thus necessary to quantify damage based on a quantifiable measure. For aesthetic damage in masonry, cracks, an expression of damage, have been selected in this study to represent light damage. The width, length, and number of cracks in a masonry structure are used to monitor the progression of damage. The appearance of cracks is employed to define the initiation of the damage, and the ease of repair is utilised to categorise the damage. Such a classification is adapted from Boscardin et al. [10], Burland et al. [11], and, at its latest,

Giardina et al. [12], and is summarised in Table 1. Further, the three categories are represented with a light damage parameter using a single scalar. This parameter, denoted Ψ, summarises precisely, using Equation 1, the intensity of the damage, such that its initiation and progression can be clearly monitored. The parameter expresses the total of visible cracks such that the narrowest visible cracks with a width of 0.1 mm result in a value of around one (Ψ=1), slightly larger cracks of close to 1 mm width correspond to two (Ψ=2) and cracks of approximately 4 mm in width give a value of three (Ψ=3).

$$\Psi = 2 \cdot n_c^{0.15} \cdot \hat{c}_w^{0.3} \text{ with } \hat{c}_w = \frac{\sum_{i=1}^{n_c} c_{w,i}^2 \cdot c_{L,i}}{\sum_{i=1}^{n_c} c_{w,i} \cdot c_{L,i}} \qquad \text{(Equation 1)}$$

Where n_c is the number of cracks in the wall/specimen, $\hat{c}_w$ is the width-weighted and length-averaged crack width (in mm) calculated with c_w (the maximum crack width along each crack in mm) and c_L (the crack length in mm). Hence, for n_c=1, $\hat{c}_w = c_w$. In this expression, the crack width of each crack is measured at their widest point. In this manner, values of Ψ lower than 1 correspond to cracks that cannot be seen with the naked eye, while when larger than 1 represent visible damage. This is herein marked as the initiation of light damage, and any increase in the Ψ parameter can be considered progression of light damage.

Table 1. Categorisation of light damage.

Category of damage	Damage		Description of typical damage and ease of repair	Approx. crack width (mm)
No damage (DS0)	Negligible	Ψ = 0	No cracks	0
	Invisible	Ψ < 1	Hairline cracks. Invisible to the naked eye.	< 0.1mm
Aesthetic damage (DS1)	Just visible	Ψ ≥ 1	Fine cracks which can easily be treated during normal decoration. Perhaps isolated slight fracturing in building. Cracks in external brickwork visible on close inspection.	> 0.1mm
	Very slight	Ψ < 2		< 1mm
Moderate damage (DS2)	Slight	Ψ ≥ 2	Cracks easily filled. Redecoration probably required. Several slight fractures showing inside of building. Cracks are visible externally and some repainting may be required externally to ensure water tightness.	> 1mm
		Ψ < 3		< 4mm
	Moderate	Ψ ≥ 3	Cracks difficult to fix, may require structural intervention.	> 4mm

3. Experimental Tests for Light Damage

Experimental tests were performed on walls and spandrels. Both types of specimens were loaded in their plane and subjected to actions causing cracks in the range within light damage.

3.1. Wall Tests

The walls were single-wythe, 3 metres wide and 2.7m tall, and most featured an opening for a window located asymmetrically. Figure 1 presents a drawing of the four types of walls while Table 2 shows an overview of all the specimens tested. The clay walls were built using bricks in the format 50x100x210mm, while the calcium-silicate walls used slightly larger bricks of 70x102x210mm; both types of walls included a precast concrete window lintel with a height of one brick. The walls were subjected to a large number of cycles in order to investigate the progression of damage when exposed to repeated, identical solicitations. The large number of quasi-static cycles with small drift values were to mimic repeating seismic events causing light damage to the masonry. Four types of walls were tested: fired-clay brick walls with an opening, similar calcium-silicate brick walls, clay masonry without an opening, and clay masonry with an opening and pre-damage. The latter consisted of plastic strips positioned in specific joints so as to simulate an existing crack due to (previous) settlement actions. The walls were loaded with a constant vertical overburden so as to produce a vertical stress of 0.12 MPa in walls with an opening, and a higher stress of 0.46 MPa in the shear walls. The first value corresponds to one concrete- or two timber-floor storeys and a timber roof, and the latter to three concrete-floor storeys and a roof. This value is on the higher side, but was necessary to maintain reliable control of the test while enforcing a double-clamped condition.

Cracks were measured using Digital Image Correlation (DIC) and became visible at a lateral drift of approximately 0.25‰ for both shear walls and walls with openings; both types of walls were tested to a drift of 0.7‰ where Ψ approached the upper boundary of what could be considered light damage. The cracks in the walls were mostly horizontal and diagonal following the masonry pattern and appeared at the interface between brick and mortar. At the later steps of the calcium-silicate walls however, the cracks also split bricks and cut vertically through these as depicted in Figure 2; this was not observed in any of the clay walls. Cracks grew in width and length not only when increasing the drift but also when the drift was kept constant. This occurred even when the drift was not reversed (one-way cyclic), but was more prominent during two-way cyclic tests. At the same time, the lateral force resisted by the walls (strength capacity) degraded approximately 5% over the first few cycles and stabilised towards the end of each step; this occurred after about 30 cycles and was thus selected as the typical cycle count in each step.

The initial crack pattern in the shear walls consisted of distributed stair-case diagonal cracks in the body of the wall, but consolidated into a single, wider diagonal crack towards the end of the tests. Conversely, the cracks in the walls with openings propagated from the four window corners, becoming longer and wider as the tests progressed. The pre-cracked joints in the pre-damaged walls only modified the crack pattern slightly but increased the intensity of the damage when compared to the virgin walls, especially at low values of drift, with up to 50% more damage on the first and second steps.

The cracks were also assessed in order to establish a range for light damage from these experiments. A linear relationship was regressed between drift and the Ψ parameter for the different walls. Then, considering the limits presented in Table 1 and one standard deviation from the linear fit, lower and upper drift boundaries for light damage were determined; these are presented in Table 3.

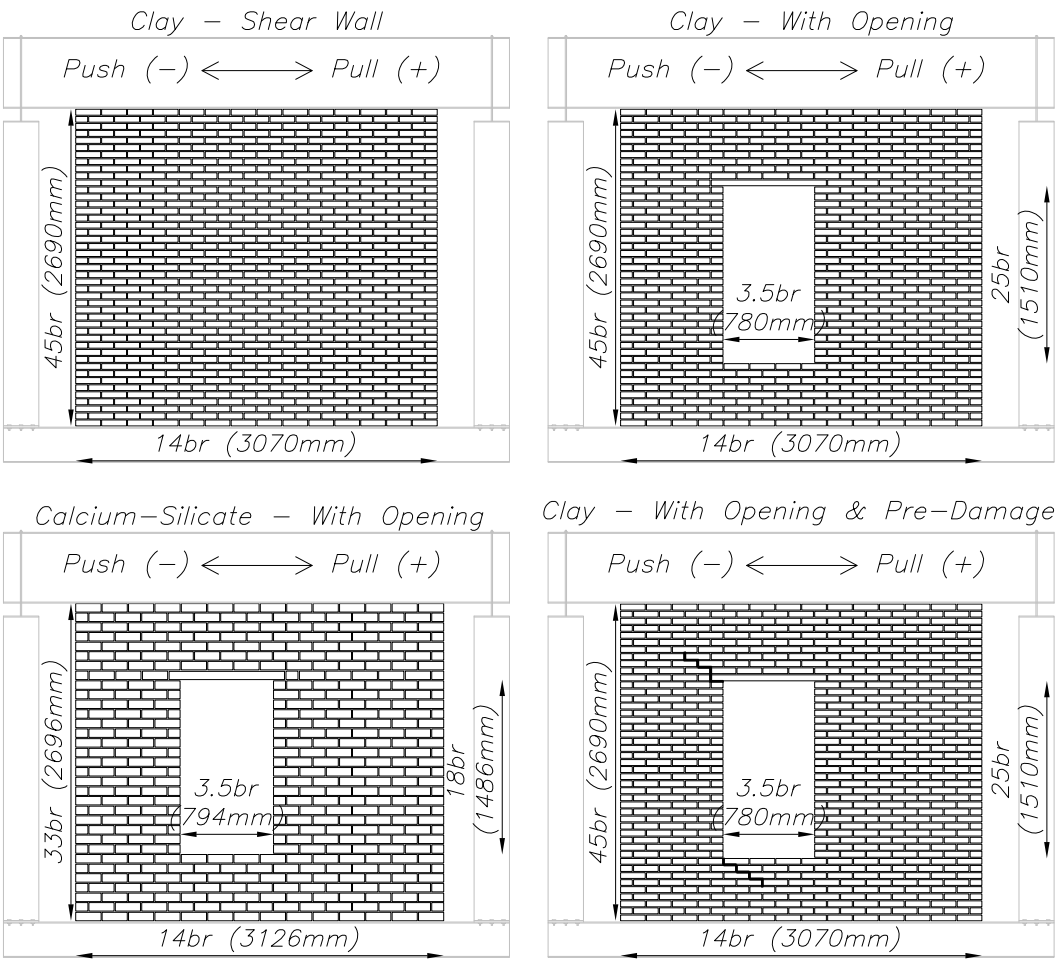

Figure 1. Drawings of the four types of wall specimens tested.

Table 2. Overview of all walls tested for the light damage investigations.

Wall iD	Wall Type	Description	Protocol	Steps & Boundary
TUD-Comp40	Clay with opening	First wall to be tested, few cycles.	5x3 one-way cyclic followed by 7x30 two-way cyclic	Drift (5): +0.26, +0.33, +0.41, +0.48, +0.55‰ Drift (7): ±0.26, ±0.33, ±0.41, ±0.48, ±0.55, ±0.63, ±0.70‰, Cantilever 0.12 MPa
TUD-Comp41		Identically-tested with a larger number of one-way cycles.	5x20 one-way cyclic followed by 7x30 two-way cyclic	
TUD-Comp42				
TUD-Comp43		The protocol was not quasi-static for the first part and the second part had a large number of cycles.	5x30 one-way cyclic (dynamic) followed by 7x50 two-way cyclic	
TUD-Comp44		Only one-way cycles tested because of error in control setup.	5x30 one-way cyclic	
TUD-Comp45	Clay with opening & pre-damage	Nominally-identical walls but including plastic strips in specific joints to simulate settlement pre-damage	5x30 one-way cyclic followed by 7x30 two-way cyclic	
TUD-Comp46				
TUD-Comp49	Calcium-Silicate with opening	Nominally-identical walls but built with calcium-silicate bricks.		
TUD-Comp50				
TUD-Comp47	Clay no opening	Shear walls tested in double-clamped condition with a high overburden.	6x10 asymmetric two-way cyclic	±0.27, ±0.33, ±0.42, ±0.49, ±0.59, ±0.70‰, Double-clamped 0.46 MPa
TUD-Comp48				

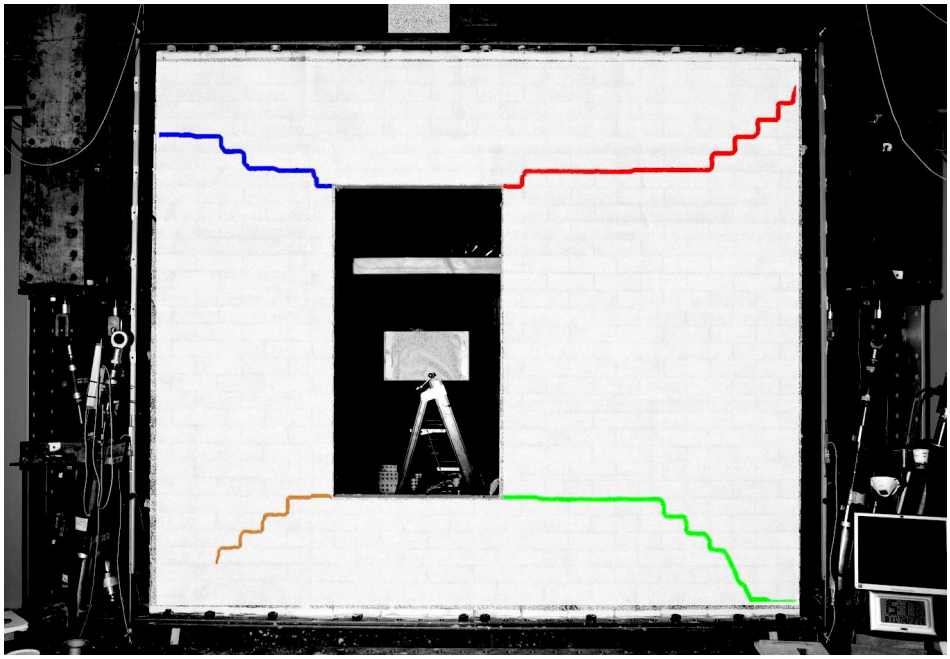

Figure 2. Calcium-silicate wall tested with final cracks highlighted.

Table 3. Summary of drift values for light damage from wall tests.

Material	Clay Brick		Calcium-silicate Brick
Behaviour	Flexural	Shear	Flexural
DS1 expected between	0.25‰	0.2‰	0.15‰
	1.1‰	0.9‰	0.65‰

3.2. Spandrel Tests

Similarly, spandrels of about 1.3m in width and half a meter in height, were configured such that a vertical crack would develop. This was to replicate vertical cracks in masonry sometimes caused by earthquakes but predominantly triggered by settlement deformations. Moreover, the vertical crack in the spandrels and the horizontal and diagonal cracks in the walls, allowed for a more complete picture of the damage behaviour of the masonry material. The spandrels, as illustrated in Figure 3, were built of fired-clay and calcium-silicate bricks, and were loaded by two jacks (F) and supported by two rollers such that a vertical bending crack developed from the top-down. The development of this crack was guided by a sensor spanning the top three joints such that the crack mouth opening displacement (CMOD) was captured if any of the three joints was the one to crack. Additionally, the tests could be performed cyclically by applying a constant counterweight force (CW) which acted against the force of the jack and allowed the loading direction to be reversed.

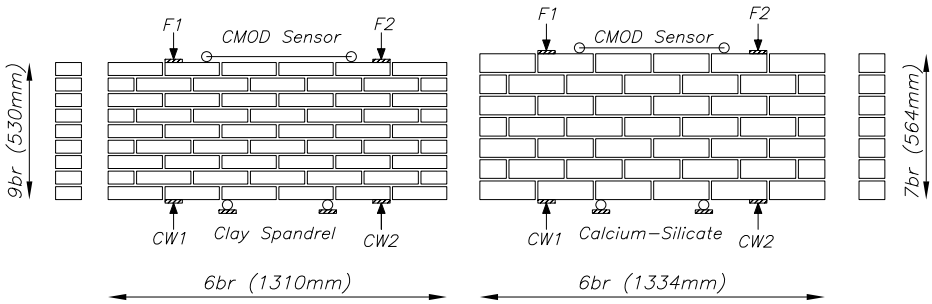

Figure 3. Spandrel and its loading scheme; fired-clay bricks (left) and calcium-silicate bricks (right).

The two material variations of the spandrels were further varied by performing some tests monotonically and others cyclically with a different sequence of loading steps. These variations are summarised in Table 4. The monotonic tests increased the CMOD at a given rate, and the cyclic tests reached a certain displacement, returned to zero (limited by zero force), and repeated the same displacement for as many cycles as were in a step. The force required to attain a certain displacement dropped with each iterative cycle, with up to an approximate 20% average decrease in the last step. This strength degradation, also observed in the walls but at a reduced intensity, is presumably caused by sliding of the bricks at the bed joints. The vertical crack in fact, zigzagged down along the head- and bed-joints producing a toothed crack in the clay specimens. For the calcium-silicate samples, however, the crack followed a straight vertical path cutting bricks in what was a brittle failure mechanism. When plotting the vertical displacements of the jacks against the force applied, the total energy input into the specimens and released by the vertical crack is displayed; then, the fracture energy can be computed for an idealised crack surface of 0.5m in height and 0.1m in width. This exercise is presented in Figure 4, where the aforementioned force versus displacement for a few representative tests is displayed; the fracture energy, Gf, is also included. This confirms that calcium-silicate tests behaved in a more brittle manner with a lower fracture energy, and verifies that the toothed crack observed in clay brick specimens allowed for a higher energy dissipation. It must be noted, however, that obtaining a fracture energy from cyclic tests is not correct and is presented here only as a comparison measure between the two materials.

Table 4. Overview of 29 spandrel tests.

Spandrel Type	Number	Description	Protocol	Steps
Clay Monotonic	4	9 tests performed monotonically at two rates of CMOD control	Monotonic (0.5 µm/s)	CMOD (max. 10 mm)
	5		Monotonic (5 µm/s)	
Clay Cyclic	3	15 successful cyclic tests with clay specimens varying the number of steps and of cycles.	3x10 + monotonic	CMOD: 50, 100, 150 µm
	7		3x30 + monotonic	
	1		1x100 + monotonic	
	4		6x15 + monotonic	50, 70, 90, 110, 120,150 µm
Calcium-silicate Cyclic	5	Cyclic tests in calcium-silicate all with the best combination of steps and cycles	3x30 + monotonic	CMOD: 50, 100, 150 µm

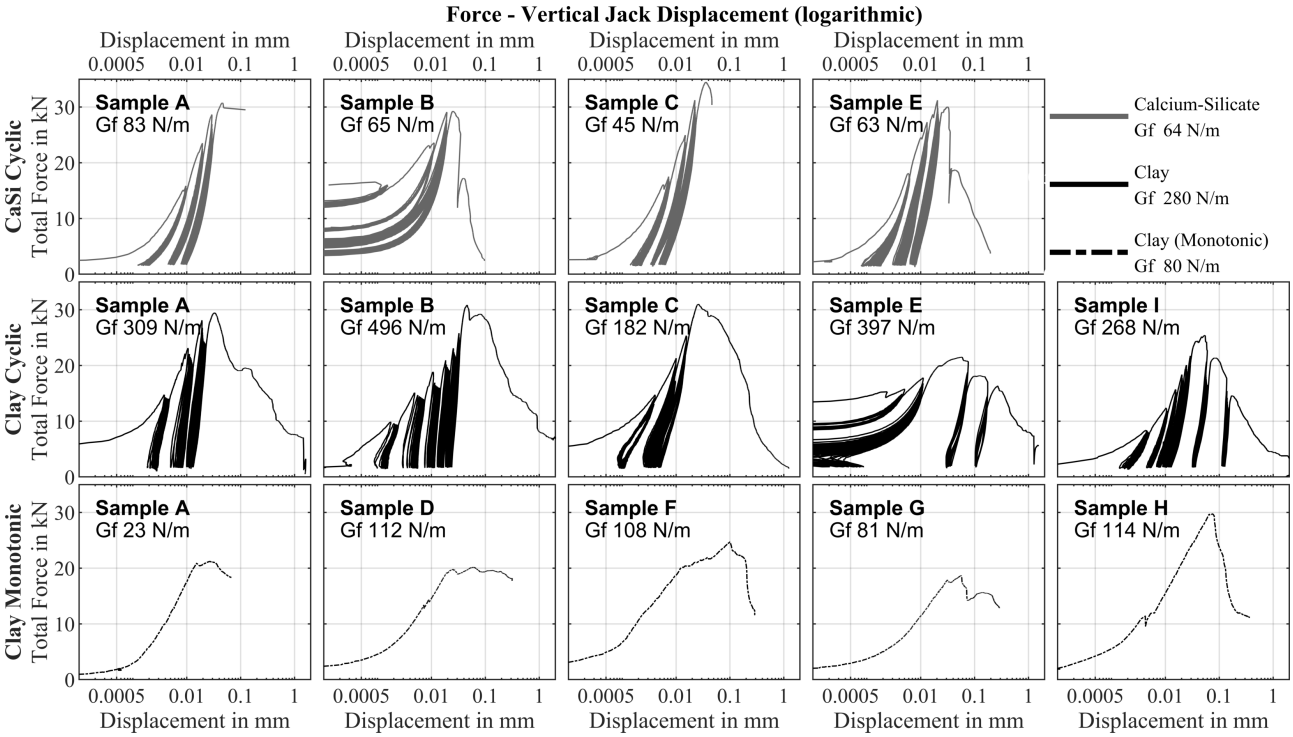

Figure 4. Total force against average logarithmic displacement of the jacks for a few tests. Note that this is not against the controlled CMOD. Values of average fracture energy shown include tests not plotted.

4. Calibration and Extrapolation Finite Element Models

4.1. Calibration Models

The experimental tests were reproduced with FE models using a non-linear material model to simulate the cracking behaviour of masonry. The orthotropic, total-strain based masonry model EMM (Engineering Masonry Model in DIANA FEA) was selected as constitutive model. This model includes different values of inelastic and elastic properties for the two main directions: the local x parallel to bed-joints and local y aligned with the head-joints. The in-plane crack directions are four: two of them are located along the joint's axes and the other two are diagonal, taking into account the masonry pattern by a parameter (angle for diagonal cracking). As failure mechanisms, the material model includes tensile cracking with softening and secant nonlinear unloading/reloading behaviour, Coulomb friction with cohesion softening and elastic unloading/reloading, and compression crushing (in both horizontal and vertical directions) with mixed secant/elastic unloading and reloading behaviour [13, 14]. The models employed a mesh size of 50 mm with quadrilateral 8-node quadratic elements (CQ16M) with 3x3 Gauss integration points.

The focus of the computations in this paper hereon will be on clay brick masonry; all clay specimens were modelled using the same set of properties for the material model, as they were also constructed from the same material. These material properties (detailed in Table 5) were partially selected from small companion tests such as bond-wrench tests, compression wallets, shear triplets and in-plane bending tests, and partially from the actual wall data. The calibrated values were varied within two standard deviations of the companion tests to assess their influence, but selected within one standard deviation to ensure a realistic set of properties. For example, the direct tensile strength, which is key for accurately determining the rocking and diagonal cracking behaviour, was varied between 0.1 and 0.2 MPa, ultimately selecting 0.16 MPa corresponding to the upper one-standard-deviation value from small scale tests. Two phases were used in the model: gravity and overburden were applied first, and the displacement field, yet not the stress field, was cleared. Then, the in-plane, displacement-controlled load was introduced in the model. The experimental protocol was employed but, in order to optimise the computational time, three cycles per step were considered as the material model does not yet include strength degradation an inputing additional identical

cycles would not have modified the results. Finally, the presence of plastic strips in the pre-damaged walls was simulated by modifying the material of the elements at the cracked positions with zero tensile strength.

The calibration of the models was performed so as to obtain the most comparable behaviour in terms of initial stiffness, strength, and hysteresis, but also crack patterns and damage intensity. Figure 5 shows an example of a crack pattern comparison. The most influential parameters were the tensile strength of the masonry composite, the fracture energy, and the relationship between the head- and the bed-joint strength. The boundaries of the walls also played a significant role, especially for the double-clamped condition. Here, the two steel beams that supported, and to which the experimental walls were glued, were included in the models as elastic steel (ρ=7.85 ton/m^3, E=210 GPa, ν=0.3) with a HEB-600 for the top and a HEB-300 profile for the bottom beams. The concrete lintel was modelled linear-elastically (ρ=2.4 ton/m^3, E=31GPa, ν=0.2). The flexural failure mechanism of windowed walls and the shear mechanism of squat walls was faithfully reproduced with the same model properties. This gives confidence that the models may be extrapolated to similar geometries while maintaining their veracity. Overall, the calibrated models can be described to be in good agreement with the experiments.

Table 5. Properties and parameters used in the material model.
(1) From experiments, (2) from calibration, and (3) from formulation $G_{f,I}=0.025\cdot(2\cdot ft)^{0.7}$

Material Properties	Units	Engineering Masonry Model Clay Masonry - Calibration	Source
Density	**kg/m³**	1.62E+03	*1*
Elastic Modulus Perpendicular to Bed-Joints	**MPa**	3.57E+03	*1*
Elastic Modulus Parallel to Bed-Joints	**MPa**	2.50E+03	*1*
Elastic Shear Modulus	**MPa**	1.50E+03	*2*
Bed-Joint Tensile Strength	**MPa**	1.60E-01	*1*
Minimum Head-Joint Tensile Strength	**MPa**	1.60E-01	*2*
Tensile Fracture Energy	**N·m/m²**	1.13E+01	*3*
Compressive Strength	**MPa**	1.29E+01	*1*
Compressive Fracture Energy	**N·m/m²**	3.56E+04	*1*
Friction angle	**rad**	6.88E-01	*1*
Cohesion	**MPa**	1.70E-01	*1*
Shear Fracture Energy	**N·m/m²**	2.09E+02	*1*
Predefined Angle for Diagonal Cracking	**rad**	5.00E-01	*1*

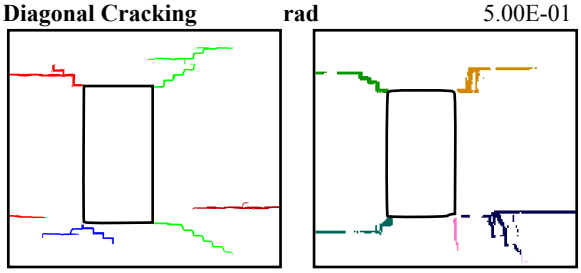

Figure 5. Comparison between detected crack pattern in the experiment of Comp46 (left) and the model of a clay wall with a window opening and pre-damage (right).

4.2. Extrapolation Models with Walls

The calibrated models were modified slightly so as to input a seismic acceleration series and perform a non-linear time-history analysis (NLTHA). First, the steel beams were removed and, at the top, a line mass of 10 ton, simulating the presence of a floor was included, while, at the bottom, a set of springs and dampers was added to mimic the support of soil, silty sand or peat. The top mass had only a dynamic influence and did not modify the overburden on the wall of 0.12MPa. The bottom interface was calibrated from other studies [9] and included, for the silty, sandy soil, a vertical stiffness modulus set to 0.44 N/mm^3 (0.57 N/mm^3 at the edges), and a constant horizontal stiffness of 0.38 N/mm^3. The vertical damping coefficient was 206 Ns/mm (6.87 Ns/mm at the edge), while the horizontal damping coefficient was set to 110 Ns/mm. A bad soil, consisting of peat, was also considered as comparison. Further, a Rayleigh damping of 2% based on the first two modes (for participating mass) was included in the dynamic models.

The accelerations corresponding to the earthquake of Zeerijp (8 January of 2018) registered at the Garsthuizen and Appingedam stations were imposed at the base of the models. These two series were used to compare the response of the models when exposed to an earthquake recorded near the epicentre or far from the epicentre, respectively; both series were scaled to various values of peak ground velocity (PGV) starting at 2 mm/s (a PGA of 65 mm/s^2 approx.). Moreover, the response of the models was recorded after applying one or multiple, identical acceleration signals. An additional variation comprised the material, which modified its stiffness, tensile strength, and fracture energy to produce three sets of masonry: poor, standard, and strong, differing about 30% in tensile strength. Further, a vertical displacement profile was applied at the bottom edge of the wall's interface mimicking a hogging settlement profile with one edge of the wall sinking deeper than the other. Depending on the magnitude of the settlement, the damage intensity of the wall, as measured with Ψ, varied between 0.5 and 1.5. Hence, unlike the calibration models were weakening of individual elements was applied to reproduce the experiments, for the extrapolation models, pre-damage was generated via pre-loading of the model. The various initial states of the models were then subjected to the imposed seismic accelerations.

In this manner, the relationship between, for instance, the initial damage or the number of seismic events and the final damage of the 2000 model permutations could be observed but, more importantly, quantified. First, expectedly, as the PGV increased, so did the final damage; after exposing some models to one earthquake of 8mm/s, they exhibited an average damage increase of 0.20Ψ, while at 16mm/s, the increase was 0.36Ψ (80% more) and at 32mm/s, it was 0.57Ψ (185%). When, however, they were exposed to two identical earthquakes of 8mm/s, the average increase was 0.22Ψ (10% more than one event); this shows that exposure to repeated earthquakes also leads to an increase in damage, albeit marginally so. Similarly, the average damage increase of the poor material was 34% higher than that of the standard material, while the stronger material was 24% less damaged on average. Additionally, models of walls starting with a low level of pre-damage ($\Psi_0 \approx 0.5$), obtained on average 12% less additional damage than completely virgin walls. This means that the initial damage helped mitigate the effect of the earthquake; note nonetheless, that the final damage value was higher than that of the virgin walls. Moreover, models of walls on peat accumulated 33% more damage than walls on the sandy soil; while, models of walls with a window attained a 25% higher increase in damage than walls without a window. And, models subjected to the record registered far from the epicentre of the earthquake displayed a 24% smaller increase in damage than those exposed to the signal recorded near the epicentre; note that both earthquakes were scaled to the same intensity and thus only the character of the record like frequency, effective cycles, and vertical acceleration, differ between them. Furthermore, the values described all refer to the increase in damage and not the final damage, as the pre-damaged models had differing initial values of damage.

4.3 Extrapolation Models with Façades

Four existing façades, identical to the ones used in the study of Van Staalduinen et al. [9] and taken from field-cases, were also modelled with an approach nominally identical to the one described in section 4.2. The only significant variation concerned the lintels of the windows. As cracks are usually found around these openings, modelling of the lintel, especially for wider openings, is paramount. Three different lintel modelling approaches were followed depending on the width of the opening, just as in the field-cases. For window or door openings narrower than one metre, no lintel is used and the masonry material is thus continuous in the model. For larger openings up to one and a half metres, a soldier lintel was considered consisting of vertical bricks; in the model, the local axes of the lintel portion was thus rotated. Finally, for larger openings, a steel beam was placed to hold the masonry such as is used in older structures; in the model, a Coulomb-friction interface is placed between the steel and the masonry. Moreover, for all façades, a masonry foundation, consisting of a thickening of the wall of 0.4m was implemented and modelled with the non-linear material model with identical parameters as the rest of the façades.

The four façades were also subjected to settlement action producing an initial damage condition, exemplified in Figure 6 for façade 2, to compare against the undamaged condition. Then, the façades were analysed with similar permutations as the extrapolation wall models comprising variations in soil, in the masonry material, and in the intensity and distance (though not repetition) of the seismic events. An example of the final damage appraisal of the façade models is depicted in Figure 7 for façades 1, 3, and 4. This also illustrates the geometry of the four façades considered.

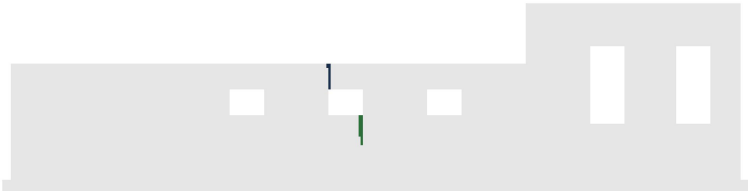

Figure 6. Settlement damage of façade 2.

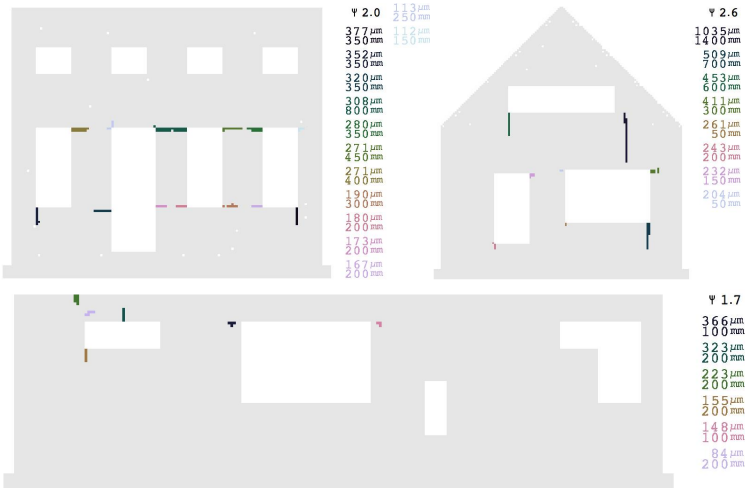

Figure 7. Final damage of three different façades on peat, near earthquake, weak material, no pre-damage, and PGV of 32 mm/s. Top, left and right, façades 1 and 3; bottom, façade 4.

Damage was observed mostly around the openings, also in the top middle of openings without lintels, and at the edges of strong lintels when these were present. Cracks developed by the settlement action were further widened and lengthened by the imposed seismic accelerations. From these analyses, on average, the façades of poor material experienced 50% more increase in damage than the ones modelled with the standard material, whereas the strong material reduced the increase in damage by 25%. Similarly, the façades placed on the good, sandy soil displayed 13% less damage increase than those on the peat. Moreover, the façades with initial damage exhibited a 40% lower increase in damage than the ones with no initial damage; however, in all cases, the final damage of the pre-damage façades was higher. Furthermore, near earthquakes caused a 28% greater damage increase than earthquake of the far type; and, a PGV of 2mm/s caused an average increase of 0.16Ψ, with 4 mm/s leading to a 14% larger increase, 8mm/s to 59% more, 16mm/s caused 2.5x the damage of a 2mm/s event and 32mm/s led to an average increase of 0.70Ψ (about 330% more than the lightest earthquake). Finally, at 32mm/s, 4% of the initially undamaged models could be considered to have exceeded light damage, while, of the models with prior settlement damage, 9% exceeded light damage at 32mm/s, 4% at 16mm/s, and 2% at 8mm/s.

In comparison, the wall models of poor material appeared less vulnerable than the façades of poor material. Moreover, the larger and more complex façades also seemed more sensitive to larger PGVs than the walls, suggesting that the greater number of openings has a negative impact towards damage. In respect to soil type and distance to the epicentre, the walls produced results that are representative of the behaviour of the façades. In general, it seems that the overall results of the wall models are in good agreement with the results obtained from the more complex façade models. In addition to the computations for clay brick reported herein, computational studies of the calcium-silicate masonry tests are currently being carried out, requiring extensions of the constitutive descriptions in order to capture the brittle splitting failures observed in the calcium-silicate bricks.

5. Earthquakes in Groningen and Estimated Light Damage

The aforementioned wall models were employed to obtain a relationship between the final damage expressed in Ψ and various model parameters. A multi-variate regression model was fitted to the data such that the

effect of each parameter combination could be represented. This model, not discussed here for conciseness, attained a good fit with a standard deviation of 0.2Ψ. This value was introduced as model uncertainty of both the regression and the finite element models. Further, each of the parameters was characterised with a probabilistic distribution. First, the material strength was varied according to results of companion tests. Then, a rough spacial distribution of masonry structures in the seismic region was used to statistically determine a uniform probabilistic distribution for both the earthquake distance and the type of soil. The latter was coupled to a microzonation soil model [15], which, based on the shear wave velocity was used to classify soil as good (sandy) or bad (peat). Finally, an equal probability was given to the presence or absence of a window. Then, for different levels of initial damage and various intensities of earthquakes (measured in PGV), the probability of developing visible light damage was computed using a Montecarlo simulation; these are summarised in Table 6. For the maximum intensity recorded to date (of approximately 32 mm/s), the probability of developing visible light damage for these fired-clay masonry structures, lies between 40% and 60%.

The simulations also show a low probability of exceeding light damage of 5% at 70 mm/s; however, since the models and analyses only consider in-plane damage and out-of-plane actions become more important at higher earthquake intensities, this value may be underestimated.

Table 6. Probabilistic estimations of light damage.

PGV	Probability of visible light damage ($\Psi \geq 1$)	
	No initial damage $\Psi_0=0$	**Light, yet imperceptible initial damage $\Psi_0 \approx 0.5$**
5 mm/s	<1%	2%
10 mm/s	1%	11%
15 mm/s	10%	33%
20 mm/s	20%	43%
30 mm/s	36%	57%
40 mm/s	51%	66%

Over the past few decades, numerous light earthquakes have been recorded in the region. In an additional simulation, the effect of repetition and the actual PGV values to which masonry structures have been exposed were considered so as to provide an estimation of the probability of light damage. For locations were a PGV of 5mm/s was exceeded at least once, the probability of displaying visible damage was 3%, but became 12% if the structures had already some initial damage ($\Psi_0 \approx 0.5$). Similarly, for locations having reached or exceeded 10mm/s, visible damage was computed to be 36% likely and 68% if imperceptible damage had already been present.

6. Conclusions

Experimental tests on fired-clay and calcium-silicate brick walls showed that visible cracks (or light damage), appear already at low in-plane drift values of 0.25‰. Moreover, the tests proved that these cracks will widen and lengthen when exposed to repeated identical actions. Additionally, the calcium-silicate walls appeared more vulnerable than clay masonry due to brittle, brick-splitting cracks. In the case of clay walls, these toothed vertical cracks give clay masonry a higher perceived fracture energy, meaning that computational models using continuum material models must consider the fracture energy to be orthotropic.

Furthermore, extensively calibrated models of the clay walls, with and without openings for windows, were extrapolated to assess seismic actions; these revealed that visible light damage is increased by repeated events, by prior existing damage of the structures, and by soft soils underneath. The relationships obtained between these parameters and light damage were then used to estimate the probability of damage at various peak ground velocity values: at 5mm/s, the probability of clay walls displaying visible damage was negligible unless these already presented some imperceivable damage, in which case the probability reached 2%; similarly, at 10mm/s, visible damage was pegged at 1% and 11% for walls with prior damage.

These estimations neglect out-of-plane actions under the premise that these are unimportant for light damage, but would be extremely relevant at higher earthquake intensities and more severe damage.

Moreover, the investigations of this study have focused on single walls, and would benefit from experimenting on larger and more complex structures while also exploring additional material variations besides the fired-clay masonry representative of older structures and masonry veneers, and the calcium-silicate brick masonry slowly offset by larger elements today. Finally, dynamic experiments and comparisons with more field-case data will help further validate the models and the observations drawn from them.

Acknowledgements

This research was funded by Nederlandse Aardolie Maatschappij (NAM) under contract number UI67339 'Damage sensitivity of Groningen masonry building structures – Experimental and computational studies', contract holders: Jan van Elk and Jeroen Uilenreef. This cooperation is gratefully acknowledged. The authors also express their gratitude to Edwin Meulman for his extensive support during the experimental phase.

References

(1) den Bezemer, T. & van Elk, J. (2018). Special Report on the Zeerijp Earthquake – 8th January 2018. NAM

(2) van Elk, J.F., Bourne, S.J., Oates, S.J., Bommer, J.J., Pinho, R. & Crowley, H. (2019). A Probabilistic Model to Evaluate Options for Mitigating Induced Seismic Risk. Earthquake Spectra · January 2019 DOI: 10.1193/050918EQS118M

(3) Messali, F., Esposito, R., Jafari, S., Ravenshorst, G., Korswagen, P.A. & Rots, J.G. (2018). A Multiscale Experimental Characterization Of Dutch Unreinforced Masonry Buildings. 16th European Conference on Earthquake Engineering, Thessaloniki 2018

(4) Esposito, R., Messali, F., Ravenshorst, G.J.P., Schipper, H.R. & Rots, J.G. (2019). Seismic assessment of a lab-tested two-storey unreinforced masonry Dutch terraced house. Bull Earthquake Eng 17, 4601–4623 (2019). https://doi.org/10.1007/s10518-019-00572-w

(5) Graziotti, F., Tomassetti, U., Kallioras, S., Penna, A. & Magenes, G. (2017). Shaking table test on a full scale URM cavity wall building. Bulletin of Earthquake Engineering, 15 (12), pp. 5329-5364

(6) Didier, M., Abbiati, G., Hefti, F., Broccardo, M. & Stojadinovic, B. (2018). Damage Quantification In Plastered Unreinforced Masonry Walls Using Digital Image Correlation. 10th Australasian Masonry Conference, 14-18 February, 2018

(7) Godio, M., Vanin, F., Zhang, S. & Beyer, K. (2019). Quasi-static shear-compression tests on stone masonry walls with plaster: Influence of load history and axial load ratio. Engineering Structures 192 (2019) 264–278

(8) Petry, S. & Beyer, K. (2015). Limit states of modern unreinforced clay brick masonry walls subjected to in-plane loading. Bull Earthquake Eng (2015) 13:1073–1095 DOI 10.1007/s10518-014-9695-9

(9) Van Staalduinen, P.C., Terwel, K. & Rots, J.G. (2018). Onderzoek naar de oorzaken van bouwkundige schade in Groningen Methodologie en case studies ter duiding van de oorzaken.. Delft University of Technology. Report number CM-2018-01, 11 July 2018 - Downloadable from www.NationaalCoordinatorGroningen.nl

(10) Boscardin, M.D. & Cording, E.J. (1989). Building response to excavation-induced settlement. Journal of Geotechnical Engineering, 115(1):1–21, 1989.

(11) Burland, J.B. & Wroth, C.P. (1974). Settlement of buildings and associated damage. Proceedings of Conference on Settlement of Structures, pages 611–654, Cambridge, 1974. Pentech Press.

(12) Giardina, G., van de Graaf, A.V., Hendriks, M.A.N., Rots, J.G. & Marini, A. (2013). Numerical analysis of a masonry façade subject to tunnelling-induced settlements. Engineering Structures 54 (2013) 234–247

(13) Rots, J.G., Messali, F., Esposito, R., Jafari, S. & Mariani, V. (2016). Computational Modelling of Masonry with a view to Groningen induced Seismicity. 10th SAHC Structural Analysis of Historical Construction, Leuven

(14) Schreppers, G.M.A., Garofano, A., Messali, F. & Rots, J.G. (2016). DIANA validation report for masonry modelling. DIANA FEA report 2016-DIANA-R1601 TU Delft Structural Mechanics Report CM-2016-17, 143 pp

(15) Kruiver, P.P., van Dedem, E., Romijn, R., de Lange, G., Korff, M., Stafleu, J., Gunnink, J.L., Rodriguez-Marek, A., Bommer, J.J., van Elk, J. & Doornhof, D. (2017). An integrated shear-wave velocity model for the Groningen gas field, The Netherlands. Bull Earthquake Eng (2017) 15:3555–3580 - DOI 10.1007/s10518-017-0105-y